AIP | Physics of Plasmas

The impact of pedestal turbulence and electron inertia on edge-localized-mode crashesa)

P. W. Xi, X. Q. Xu, and P. H. Diamond

Citation: Physics of Plasmas (1994-present) **21**, 056110 (2014); doi: 10.1063/1.4875332
View online: http://dx.doi.org/10.1063/1.4875332
View Table of Contents: http://scitation.aip.org/content/aip/journal/pop/21/5?ver=pdfcov
Published by the AIP Publishing

The impact of pedestal turbulence and electron inertia on edge-localized-mode crashes[a)]

P. W. Xi,[1,2,b)] X. Q. Xu,[2] and P. H. Diamond[3,4]
[1]FSC and State Key Lab of Nuclear Physics & Technology, Department of Physics, Peking University, Beijing 100871, China
[2]Lawrence Livermore National Laboratory, Livermore, California 94550, USA
[3]WCI Center for Fusion Theory, National Fusion Research Institute, Daejeon, South Korea
[4]Center for Astrophysics and Space Sciences and Department of Physics, University of California San Diego, La Jolla, California 92093-0429, USA

(Received 22 November 2013; accepted 9 March 2014; published online 7 May 2014)

We demonstrate that the occurrence of Edge-Localized-Modes (ELM) crashes does not depend only on the linear peeling-ballooning threshold, but also relies on nonlinear processes. Wave-wave interaction constrains the growth time of a mode, thus inducing a shift in the criterion for triggering an ELM crash. An ELM crash requires the P-B growth rate to exceed a critical value $\gamma > \gamma_c$, where γ_c is set by $1/\bar{\tau}_c$, and $\bar{\tau}_c$ is the averaged mode phase coherence time. For $0 < \gamma < \gamma_c$, P-B turbulence develops but drives enhanced turbulent transport. We also show that electron inertia dramatically changes the instability threshold when density is low. However, P-B turbulence alone cannot generate enough current transport to allow fast reconnection during an ELM crash.
 [http://dx.doi.org/10.1063/1.4875332]

I. INTRODUCTION

An understanding of the periodic burst of Edge-Localized-Modes (ELMs)[1] at the H-mode pedestal is of crucial importance to present and future tokamaks such as ITER.[2] ELMs are believed to be triggered mainly by ideal MHD instabilities. The peeling-ballooning model[3] relates the onset of ELMs to linear peeling-ballooning modes, which are driven unstable by large pedestal current and pressure gradients. The peeling-ballooning model provides a simple, widely used criterion for the onset of ELMs. For a given equilibrium, if the maximum linear growth rate of peeling-ballooning modes is positive, then an ELM crash is predicted.

However, there are many experiments that cannot be explained by this linear peeling-ballooning model. In these experiments, it is found that before the ELM crash, the pedestal gradient has already crossed the linear stability boundary and is deep into the linearly unstable region.[4] Measurements from ASDEX-U show that edge profiles reached their final shape a long time prior to when the next ELM occurs, which is not consistent with the peeling-ballooning model.[5] Moreover, according to the EPED model,[6] there is kinetic ballooning mode (KBM) turbulence in the pedestal prior to an ELM crash. Thus, the impact of pedestal turbulence on ELM crashes is an interesting issue to investigate.

Another issue important to ELM dynamics is related to hyper-resistivity. In a previous study, hyper-resistivity was demonstrated to be necessary for fast reconnection during the ELM crash.[7] Without hyper-resistivity, the current layer which forms will eventually be smaller than the grid resolution, so the simulation fails. However, in the previous study, hyper-resistivity was not determined self-consistently, but based on theoretical motivated estimates. Considering the importance of hyper-resistivity to ELM crashes, nonlinear ELM simulations with self-consistent hyper-resistivity are necessary to obtain a better understanding of ELM dynamics.

In this paper, these questions are studied via numerical simulations by using the global two-fluid simulation code BOUT++.[8] We demonstrate that once the pedestal becomes linearly unstable to peeling-ballooning modes, ELMs are not triggered immediately. Instead, a state of self-generated turbulence develops. The pedestal can keep evolving to higher pressure gradient because the background turbulence will interrupt the rapid growth of linear instability via nonlinear mode coupling. Finally, ELMs are triggered once the maximum linear growth rate of the system satisfies a new relation $\gamma > \gamma_c$, where γ_c is the critical growth rate, which is determined by the ambient background turbulence.[9]

We also studied the linear and nonlinear impacts of electron inertia as a means to realize hyper-resistivity. When density is low, electron inertia dramatically destabilizes peeling-ballooning modes and reduces the threshold for instability. With P-B turbulence, electron inertia can generate current transport, but this is still not enough to allow an ELM crash. Our results indicate that successful nonlinear ELM simulations with self-consistent hyper-resistivity need to include pre-existing micro-turbulence and, thus, this problem is intrinsically a multiscale one.

The remainder of the paper is organized as follows: Sec. II describes the nonlinear ELM model and Sec. III describes the impact of electron inertia. Section IV is the summary and discussion.

[a)]Paper YI2 2, Bull. Am. Phys. Soc. **58**, 365 (2013).
[b)]Invited speaker.

II. NONLINEAR ELM MODEL

A. Simulation model and equilibriums

The well-benchmark BOUT++ (Ref. 8) 3-field nonlinear reduced MHD model[7] is employed in this work. The equations and definitions are as follow:

$$\frac{d\varpi}{dt} = B\nabla_\parallel J_\parallel + 2\mathbf{b}_0 \times \kappa \cdot \nabla\tilde{P} + \mu_{i\parallel}\nabla_\parallel \varpi - \frac{1}{2\omega_{ci}}\{\nabla_\perp^2[\phi_T, P_i] - [\nabla_\perp^2\phi_T, P_i] - [\phi_T, \nabla_\perp^2 P_i]\}, \quad (1)$$

$$\frac{d\tilde{P}}{dt} + \mathbf{V}_E \cdot \nabla P_0 = 0, \quad (2)$$

$$\frac{\partial A_\parallel}{\partial t} = -\partial_\parallel \phi_T + \frac{\eta}{\mu_0}\nabla_\perp^2 A_\parallel - \frac{\eta_H}{\mu_0}\nabla_\perp^4 A_\parallel, \quad (3)$$

$$\varpi = \frac{\rho_0}{B_0}\left(\nabla_\perp^2\phi + \frac{1}{n_0 e}\nabla_\perp^2 P_i\right), \quad (4)$$

$$J_\parallel = J_{\parallel 0} - \frac{1}{\mu_0}\nabla_\perp^2 A_\parallel, \quad (5)$$

where $d/dt = \partial/\partial t + \mathbf{V}_{ET}\cdot\nabla$, $\mathbf{V}_{ET} = \mathbf{b}_0 \times \nabla\phi_T/B_0$, $\phi_T = \phi_0 + \phi$, $\nabla_\parallel F = B\partial_\parallel(F/B)$, $\partial_\parallel = \mathbf{b_0}\cdot\nabla + \tilde{\mathbf{b}}\cdot\nabla$, $\tilde{\mathbf{b}} = \nabla A_\parallel \times \mathbf{b_0}/B$, and $\kappa = \mathbf{b}\cdot\nabla\mathbf{b}$ is curvature. Resistivity and hyper-resistivity are fixed to be $S = \mu_0 R_0 v_A/\eta = 2\times10^{10}$ and $\alpha_H = \eta_H R_0^2/\eta = 10^{-4}$. The equilibrium $\mathbf{E}\times\mathbf{B}$ flow is assumed to balance the ion diamagnetic flow, so we have $\phi_0 = -P_0/2n_0 e$. Additional gyroviscous terms are included,[10] where $\omega_{ci} = eB/m_i$, $P_i = P/2$, and $[f,g] = \frac{\mathbf{b}\times\nabla f}{B}\cdot\nabla g$ is the Poisson bracket. The role of ion diamagnetic effects on peeling-ballooning modes is well discussed in Refs. 7 and 10, while electron diamagnetic effects are not included. This set of equations can describe the nonlinear evolution of peeling-ballooning modes and the following ELM crash.

Resistivity, hyper-resistivity, and parallel viscosity are fixed to be $S = \mu_0 R_0 v_A/\eta = 2\times10^{10}$, $S_H = \mu_0 R_0^3 v_A/\eta_H = 2\times10^{14}$, and $\mu_{i\parallel} = 0.1\omega_A R^2$, respectively. The shifted circular equilibrium, we use has minor radius $a = 1.22\,\mathrm{m}$, major radius $R_0 = 3.53\,\mathrm{m}$, and toroidal magnetic field $B_t = 1.99\,\mathrm{T}$. The profiles for equilibrium pressure P_0 and safety factor q are plotted in Fig. 1(a). The normalized pressure gradient is $\alpha = -2\mu_0 q^2 R_0 P_0'/B^2 = 2.17$ and magnetic shear is $s = rq'/q = 3.81$ at the peak pressure gradient location. This equilibrium is linearly unstable to peeling-ballooning modes. The linear growth rates and real frequencies are plotted in Figs. 1(b) and 1(d). The most unstable mode has toroidal mode number $n = 20$ with normalized linear growth rate $\gamma/\omega_A = 0.034$. According to peeling-ballooning theory, this equilibrium will have an ELM crash, because it is unstable to P-B modes.

B. Single-mode-simulation (SMS) and multiple-mode-simulation (MMS)

1. Simulation results

If the linear P-B model is correct, the initial condition should not change the result, so long as the initial

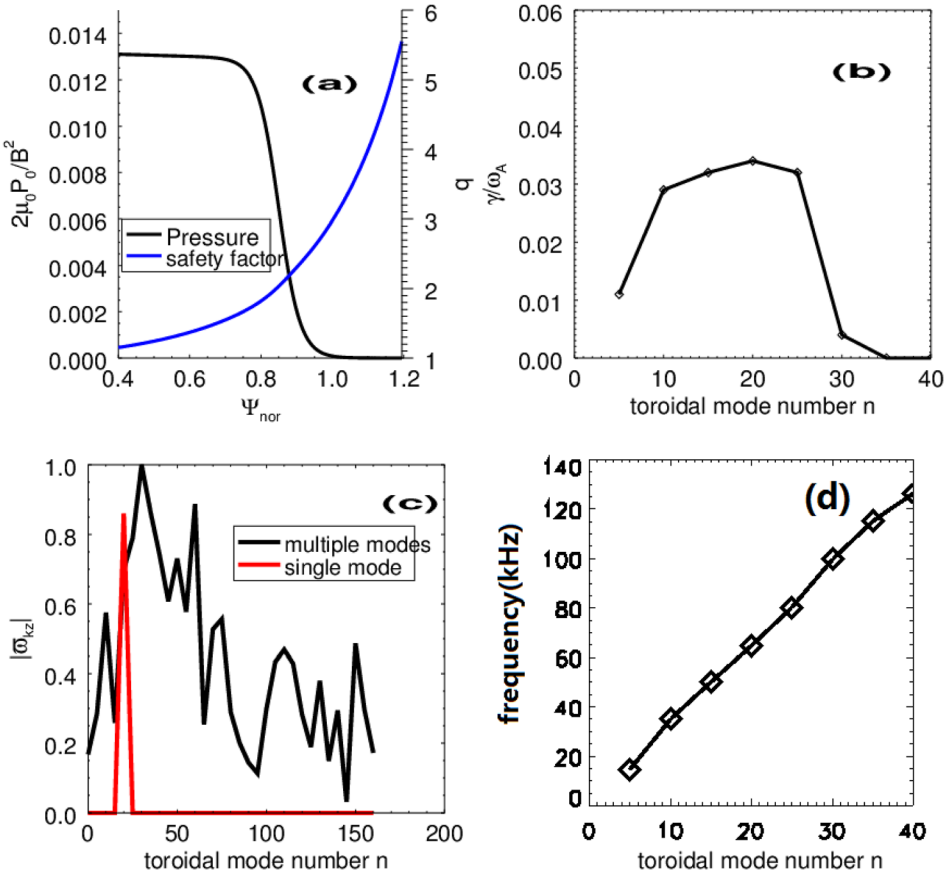

FIG. 1. (a) Pressure (black) and safety factor q (blue) profile; (b) linear growth rates versus toroidal mode number; (c) toroidal spectrum of the initial perturbation for single-mode-simulation (red) and multiple-mode-simulation (black); (d) real frequency versus toroidal mode number.

perturbation has a small amplitude. We tested this point by comparing two different initializations. The two cases are called SMS and MMS, where the initial perturbations for SMS and MMS are defined as follow:

$$SMS \quad \tilde{f}_{t=0} = f_0 G_1(\psi) G_2(\theta) \cos n\zeta, \tag{6}$$

$$MMS \quad \tilde{f}_{t=0} = f_0 G_1(\psi) G_2(\theta) \sum_{n=0}^{160} A_n \cos(n\zeta + \varphi). \tag{7}$$

Here, ψ, θ, and ζ are the radial, poloidal, and toroidal coordinate, respectively. Considering the localized nature of peeling-ballooning modes, G_1 and G_2 are set to be Gaussian functions. In SMS, the initial perturbation has toroidal mode number n = 20, which is the most unstable mode. In MMS, the initial perturbation is a toroidal spectrum with random amplitude and phase. In both cases, the initial perturbation has amplitude of $\delta p/p_0 = 10^{-4}$ set by f_0, so they both start from the linear phase. To save simulation time and increase the efficiency, a toroidal segment with n = 5 is used in our simulation, so the modes we simulate are $n = 5i$, where i is a integer from 0 to 32.

The evolution of pressure perturbations at the outer mid-plane is shown in Fig. 2 for SMS (a)–(c) and MMS (d)–(f). Note that only 1/5 of the whole torus is shown here. In the linear phase ($t = 10\tau_A$; here, $\tau_A = 3.5 \times 10^{-7} s$ is the Alfvén time), SMM has a well-defined toroidal pattern with mode number n = 20 (Fig. 2(a)), while in MMS, the pattern is dominated by n = 20 but is disrupted by other modes (Fig. 2(d)). In the early nonlinear phase ($t = 130\tau_A$), an ELM crash occurs in SMS as shown in Fig. 2(b), where the radial separation of positive and negative perturbations represents the generation of filaments and the pedestal collapse. The positive perturbation moves outward and forms filaments. Simultaneously, the negative perturbation moves inward and causes the collapse of the pressure profile. However, in MMS, the perturbation evolves into a turbulent state with random fluctuation distribution, as shown in Fig. 2(e). No filaments are generated, so there is no ELM crash in MMS. As the perturbation evolves into the late nonlinear phase, both cases show a turbulent state but with different spatial distributions. In SMS, positive and negative perturbations are completely separated and widely extended in radial (Fig. 2). In MMS, the turbulence does not radially extended and is localized near peak pressure gradient.

Unlike the original definition of 3D filaments, which are widely considered to be finger-like structures;[3,11] here, we define the 3D filament as the coherent helical perturbation, which moves and bursts outward, as shown in experimental observations.[12] The 3D structures of the pressure perturbation are shown in Fig. 3. For SMS, the perturbation satisfies this definition. But, for MMS, the perturbation does not have coherent structure along field lines and it does not move outward. We can classify the turbulent perturbations in MMS as P-B turbulence, because it is driven by peeling-ballooning modes.

Figure 4(a) shows the time evolution of ELM size, which measures the energy loss during the ELM crash and is defined as

$$\Delta_{ELM}(t) = \frac{\int_{\Psi_{out}}^{\Psi_{in}} d\Psi \oint\oint J d\theta d\zeta \left(P_0 - \langle P(t) \rangle_\zeta\right)}{\int_{\Psi_{out}}^{\Psi_{in}} d\Psi \oint\oint J d\theta d\zeta P_0}. \tag{8}$$

Here, Ψ_{in} is the inner boundary of the simulation domain and Ψ_{out} is chosen to be the location of the peak pressure gradient. In SMS, a typical ELM crash occurs at $t = 115\tau_A$, as indicated by the sudden increase in ELM size. This is consistent with linear theory. However, in MMS, an ELM crash

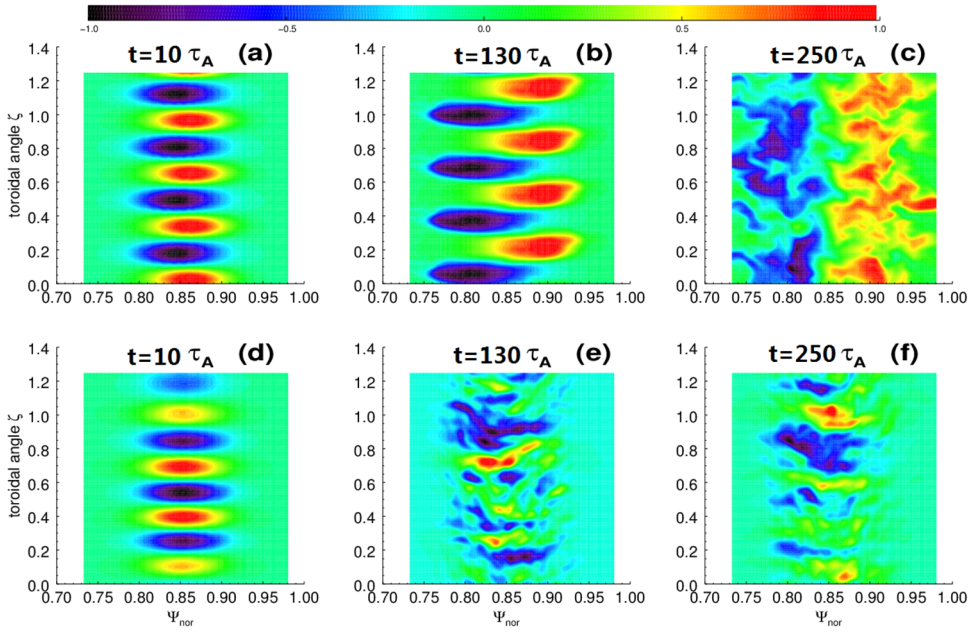

FIG. 2. Pressure perturbation at the outer mid-plane for SMS (a)–(c) and MMS (d)–(f) at three different times. The toroidal segment is 5.

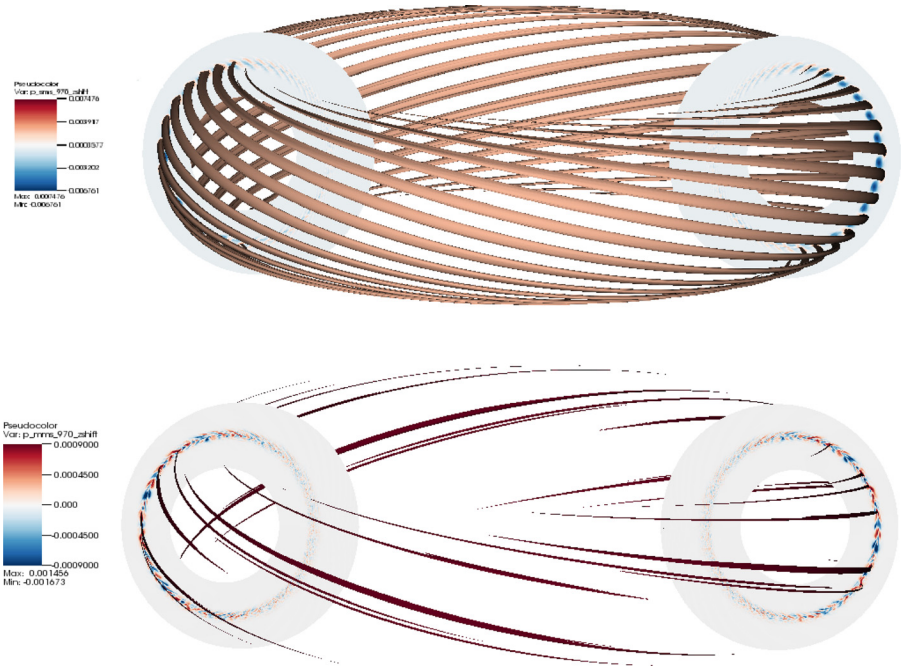

FIG. 3. The isosurfaces show the 3D structure of the pressure perturbations in SMS (upper) and MMS (lower) at $t = 140\tau_A$.

does not appear, but is replaced by slower turbulent transport. The energy loss for MMS is dramatically reduced, as compared with that for SMS. Clearly, MMS results disagree with the linear P-B theory of ELM crashes. Figure 4(b) shows the evolution of the pressure profile, where we can see a clear collapse in SMS, while the profile remains unchanged in MMS. SMS is consistent with the linear peeling-ballooning model, but MMS is not. These results show that the existence of linear instability is not sufficient for predicting ELM crashes.

2. Phase coherence time

More understanding of the difference between SMS and MMS can be obtained from considering the evolution of different modes. From Fig. 5, it is obvious that a peak at n = 20 appears in SMS at $t = 250\tau_A$. But, in MMS, there is no such peak, which means no mode is dominant in MMS. The different spectra are the result of different modes evolution.

In SMS, since only the n = 20 mode is initialized, it can grow to a large amplitude without any interruption prior to the ELM crash, as shown in Fig. 6(a). Note that before the ELM crash, only harmonics of the n = 20 mode appear and these harmonics nearly disrupt the n = 20 mode. Other modes are excited non-linearly at the ELM crash. In MMS, all modes grow simultaneously, as shown in Fig. 6(b), and the linear phase is much shorter than for SMS. Thus, no single mode has enough time to grow to large amplitude. In this

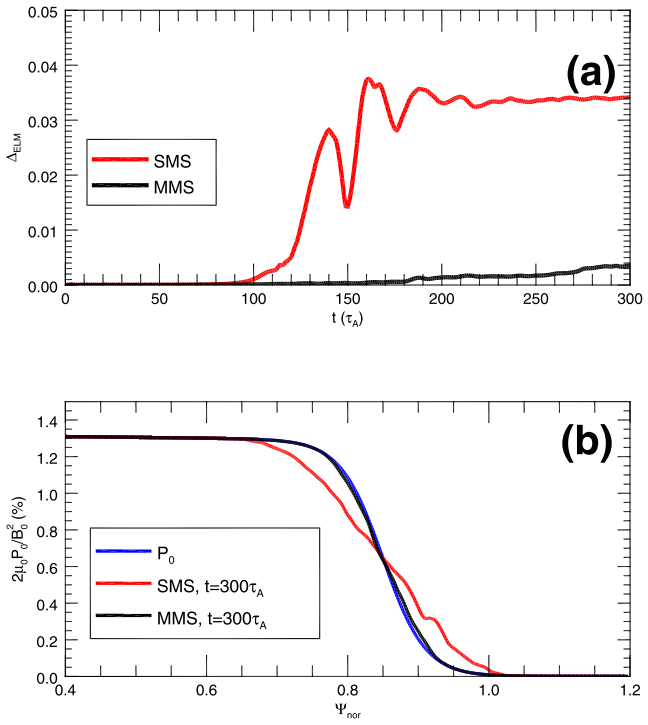

FIG. 4. (a) Time evolution of ELM size for SMS (red) and MMS (black); (b) total pressure profiles at $t = 300\tau_A$ for SMS (red) and MMS (black). Blue curve is the equilibrium pressure profile.

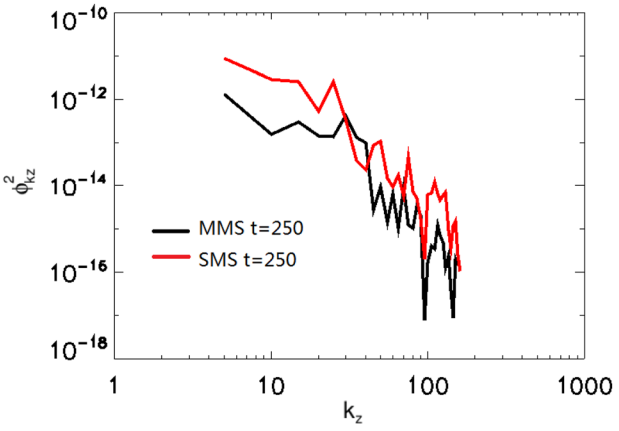

FIG. 5. The toroidal spectrum of potential at $t = 250\tau_A$ for SMS (red) and MMS (black).

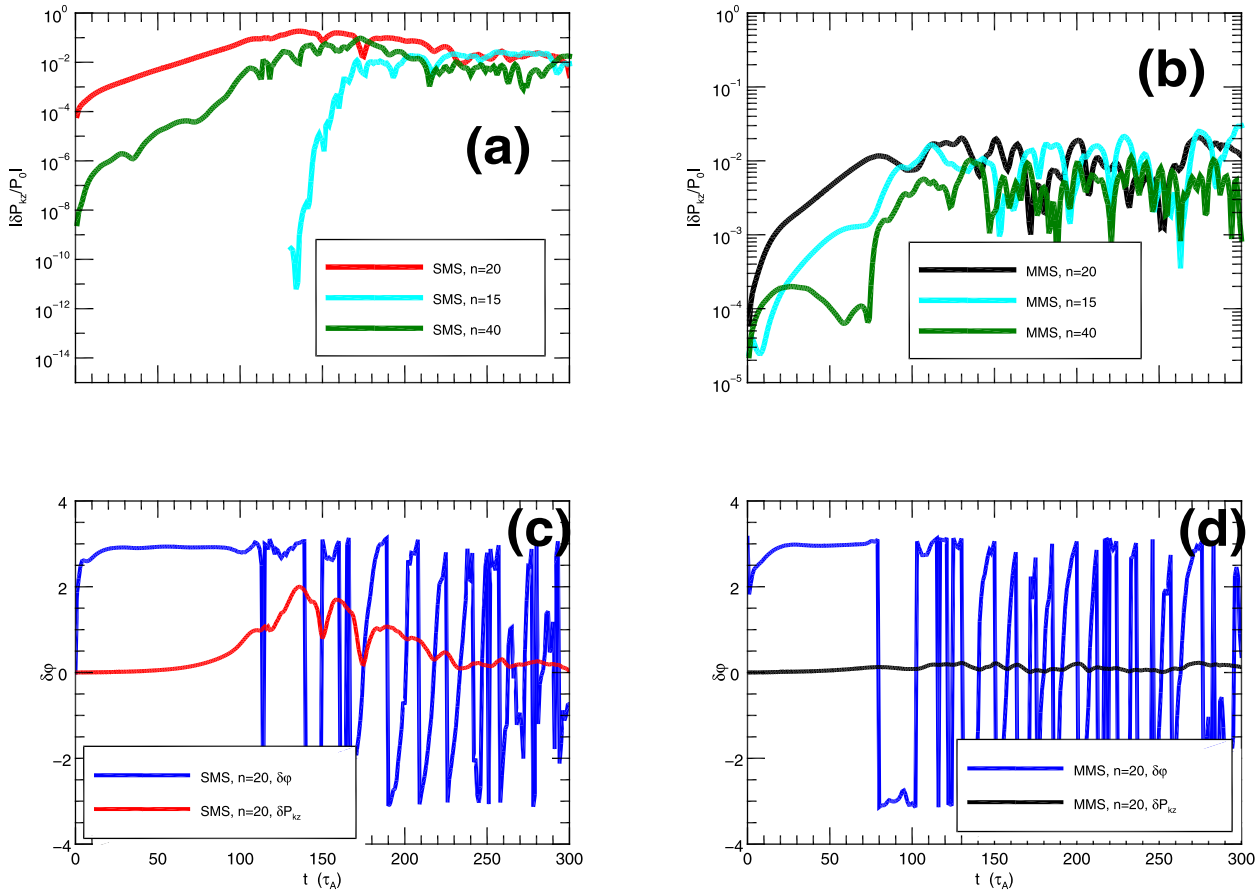

FIG. 6. (a) Time evolution of n = 20 (red), n = 15 (blue), and n = 40 (green) modes in SMS; (b) time evolution of n = 20 (red), n = 15 (blue), and n = 40 (green) modes in MMS; (c) evolution of relative phase $\delta\varphi$ (blue) in SMS; (d) evolution of relative phase $\delta\varphi$ (blue) in MMS.

way, the ELM crash event is replaced by a state of P-B turbulence. This result implies that the growth time of a mode is important to the ELM crash.

The difference between SMS and MMS can be explained using the flow chart shown in Fig. 7. To trigger an ELM crash, the P-B perturbation must grow to a large amplitude to lead to magnetic reconnection. The growth of the mode depends on both linear drive and nonlinear mode interaction. For a sufficient linear drive, both finite growth rate and a sufficiently long growth time are required. According to our model and equilibrium, the linear drive is dominated by the pressure gradient, thus the curvature term in Eq. (1) determines the linear growth rate. For a mode to extract the free energy from the equilibrium pressure gradient via the curvature term, pressure and potential perturbations must sustain the phase relation favorable to growth. Here, we define the relative phase between pressure and potential perturbation as $\delta\varphi(n,\psi,\theta,t) = \arg(\hat{P}_n(\psi,\theta,t)/\hat{\phi}_n(\psi,\theta,t))$, $\delta\varphi \in [-\pi,\pi]$, where $\hat{P}_n$ and $\hat{\phi}_n$ are the n^{th} toroidal Fourier component of the pressure and potential perturbations, respectively. The relative phase is important because it determines whether or not the ballooning mode extracts free energy from the pressure gradient. According to Eq. (1), the dependence of the kinetic energy $\tilde{V}^2_{E\times B,n}$ on the relative phase is

$$\frac{\partial \tilde{V}^2_{E\times B,n}}{\partial t} \propto -2\Re(in\hat{\phi}^*_n \hat{P}_n \mathbf{b}_0 \times \kappa \cdot \nabla\zeta) \propto \sin\delta\varphi. \quad (9)$$

Thus, the curvature term drives ballooning modes when $0 < \delta\varphi < \pi$ (phase for growth) and damps ballooning mode when $-\pi < \delta\varphi < 0$ (phase for damping). The time duration with positive $\delta\varphi$ determines the growth time for the linear drive, and thus is defined as the phase coherence time (PCT) $\tau_c(n)$. In linear theory, since there is no mode interaction, an unstable mode has infinitely long PCT, i.e., $\tau_c \to \infty$. This

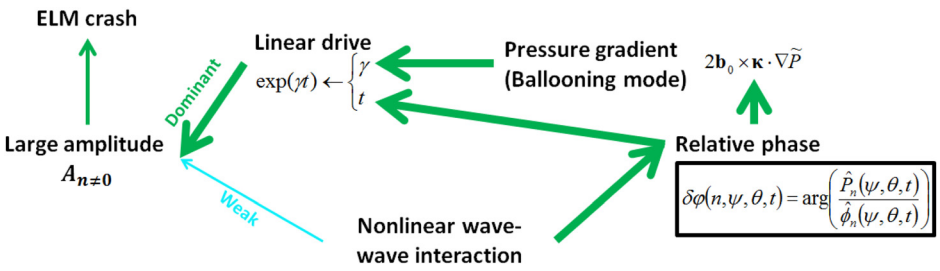

FIG. 7. Schematic plot for the role of linear and nonlinear drives in an ELM crash.

means any unstable mode will be able to grow to large amplitude if the free energy source is maintained.

The mode amplitude also depends on wave-wave interaction. However, in this model, we find that the mode amplitude is mainly set by the linear drive, while the energy transfer among different modes is relatively weak. This is verified by the strong consistency between the positive relative phase and mode growth shown in Figs. 6(c) and 6(d). However, we notice that nonlinear wave-wave interaction not only changes the amplitude of different modes, but also scatters the relative phase. Such scattering naturally induces phase fluctuations and leads a statistically distributed τ_c, which is determined by the probability distribution function of phase fluctuations $\delta\varphi$. Thus, the growth time of a mode is also determined by nonlinear mode interaction.

The measurement of the possibility distribution function (PDF) of the phase is an interesting issue because it is indicative of the nonlinear interactions in the system. However, to obtain a smooth, well converged PDF needs a lot of simulation data and is very, very laborious and expensive. To get a smooth PDF, we need to do an ensemble average. For the case of PB turbulence, since the turbulence reaches a saturated state, we can use a time average to replace the ensemble average. So, we can get a smooth PDF for the PB turbulence case, so long as the simulation is long enough. However, for cases with an ELM crash, we cannot use a time average to replace the ensemble average, on account of the crash event. In this situation, we must repeat the nonlinear simulation to get enough data points.

In addition, since the PCT is a statistical quantity, the occurrence of ELMs is not a purely deterministic process. There is no accurate exact criterion for the onset of ELM crashes. In other words, once the pedestal is unstable to P-B modes, an ELM crash can occur over a range of times, and with different probability. Note that the growth of PB modes is on the Alfvén time scale, thus a longer observation period can reduce the stochastic characters of the ELM crash. Equivalently, if one observes from a longer time, one is more likely to see an ELM crash for an unstable pedestal. When we observe the evolution of pedestal on a pedestal transport time scale, P-B turbulence has a long enough time to sample an ensemble of phase coherence times with finite probabilities. So, within a transport time scale, the mean phase coherence time $\bar{\tau}_c$ determines the averaged evolution of PB turbulence.

Overall, linear theory ignores this constraint due to τ_c, which leads to a underestimate of the growth rate for the onset of ELMs. The linear criterion $\gamma > 0$ for the onset of ELMs is a necessary but not sufficient condition.

C. Nonlinear criterion of the onset of ELMs

When the pedestal is unstable to P-B modes, turbulence is generated at first. Thus, we take the turbulent state of MMS at $t = 200\tau_A$ as the initial perturbation. Considering the fact that ELM crashes occur in most H-mode discharges, the transport caused by the P-B turbulence is typically weaker than the heat flux from the core. Thus, the pedestal gradient can evolve and steepen until a crash is triggered. The self-consistent simulation of this process requires a flux driven code, which can simulate PB turbulence on a pedestal transport time scale. Leaving this complicated matter to future work; here, we model the evolution of the pedestal pressure profile by scanning a range of initial pressure gradients with other profiles fixed. The normalized pressure gradients for different cases are shown in Fig. 8(a), where the black curve with $\alpha = 2.17$ is used in previous SMS and MMS.

The increase of pressure gradient not only increases the linear growth rate, but also changes the shape of the growth rate spectrum. Unlike the linear P-B theory, where only the linear growth rate itself is thought to be important; in our nonlinear model, the evolution of pedestal fluctuations also depends on the shape of the growth rate spectra. Different spectra can leads to different ELMs evolution.

When the pressure gradient increases, the evolution of the fluctuations can be quite different, depending upon the product of $\gamma(n)\bar{\tau}_c(n)$. Three relevant possibilities are: (a) P-B turbulence: $\gamma(n)\bar{\tau}_c(n) < \ln 10$, for all n; (b) Isolated crash: $\gamma(n)\bar{\tau}_c(n) > \ln 10$, for $n = n_d$ and $\gamma(n)\bar{\tau}_c(n) < \ln 10$, for $n \neq n_d$; (c) Turbulent crash: $\gamma(n)\bar{\tau}_c(n) > \ln 10$, for multiple n. The value ln10 is used to measure whether the mode can grow by an order of magnitude. Transport from P-B turbulence can be enhanced by the higher pressure gradient, and finally balance the heat flux from the core. In this situation, an ELM-free H-mode is obtained with an MHD turbulent pedestal. Thus, our results provide a possible explanation for ELM-free H-mode. In the situation of an isolated crash, the mode with mode number n_d is called the dominant mode, because only this mode grows to a large

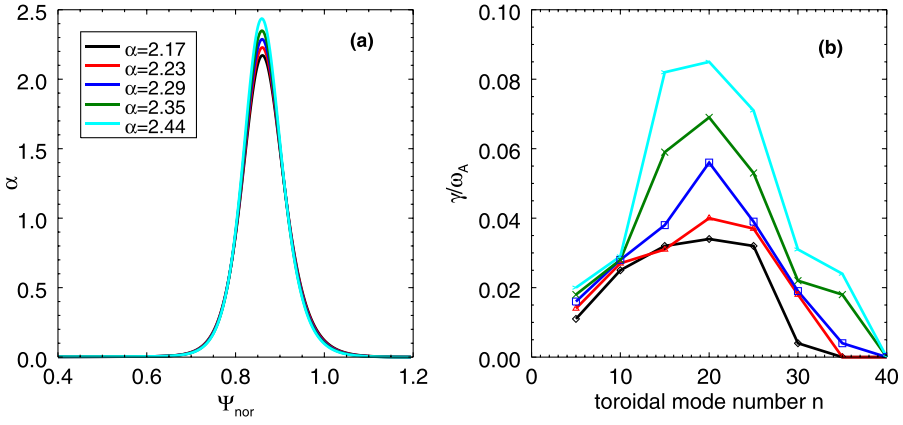

FIG. 8. (a) α profiles; (b) linear growth rates versus toroidal mode number.

amplitude, and triggers the crash. The dominant instability is determined by both $\gamma(n)$ and $\tau_c(n)$. Dominance does not necessarily correspond to the most linearly unstable mode. If several modes can develop a long PCT at the same time and grow together, we can also observe a large crash, which is a "turbulent crash."

Note that the growth rate spectrum $\gamma(n)$ and phase coherence time $\tau(n)$ are not independent, but have a strong relation. The phase coherence time, in fact, measures how long a mode can sustain its own coherence pattern for mode growth. Obviously, a mode with relatively larger amplitude has larger "inertia" with which to sustain such a pattern. The mode amplitude depends its growth rate $\gamma(n)$, thus the phase coherence time must depend on the linear growth rate spectrum. Consequently, when the pressure gradient increases, both the linear growth rate and the phase coherence time change.

Figure 9 shows the evolution of pressure perturbations at the outer mid-plane for two different cases. Both cases start from the same turbulent state. For the case with $\alpha = 2.29$, the P-B turbulence evolves and has modest radial extent. No filamentary structure is generated, in this case. So this is a case with P-B turbulence. Only for the case with $\alpha = 2.44$, we can see a clear ELM crash at $t = 225\tau_A$. One important point, here, is that the most unstable linear mode, in this case, is $n = 20$, but the generated filament is $n = 15$ and the negative perturbation has $n = 20$. This result shows that the triggering of ELMs and the generation of filamentary structure are two different processes. The filaments do not always correspond directly to the most unstable mode. They depend on both linear instability and nonlinear mode interaction.

Overall, our results demonstrate that the onset of an ELM crash depends on both linear growth rate and the PCT. For an ELM crash, the condition $\gamma\bar{\tau}_c > \ln 10$ should be satisfied. This condition is equivalent to one constraint on the linear growth rate $\gamma > \gamma_c$, where $\gamma_c \sim \ln 10/\bar{\tau}_c$ is the critical growth rate. In Fig. 10(a), the maximum growth rates versus different pressure gradients for $\gamma_c/\omega_A \sim 0.075$ are plotted. Unlike the linear criterion $\gamma > 0$, our novel criterion is a nonlinear criterion, which depends on both linear instability and nonlinear mode interaction, i.e., τ_c.

We arrive at a new picture of the onset of ELM crashes. In Fig. 10(b), the black curve is the linear instability boundary. Here, we must emphasize that, in principle, this is not simply the ideal MHD instability boundary with ion diamagnetic effects alone. The linear instability boundary should include all those linear physics relevant to ELMs, like resistivity, hyper-resistivity, electron inertia, and so on. Based on this linear boundary, the nonlinear mode interaction will produce a nonlinear boundary, as shown in blue. Note that the linear boundary sets a deterministic threshold; however, the nonlinear boundary is probabilistic. With heating sources, the pedestal first evolves from within the linearly stable regime and crosses the linear boundary. ELM crashes do not occur when the pedestal is linearly unstable, but rather P-B turbulence is generated. The P-B turbulence causes turbulent transport. If the transport is weaker than the heating, the pedestal will continue to evolve and eventually cross the nonlinear boundary. At this point, an ELM crash is triggered, within a pedestal transport time scale. It is also possible that the enhanced turbulent transport balances the heating, so the pedestal stops evolving and stays in the turbulent state

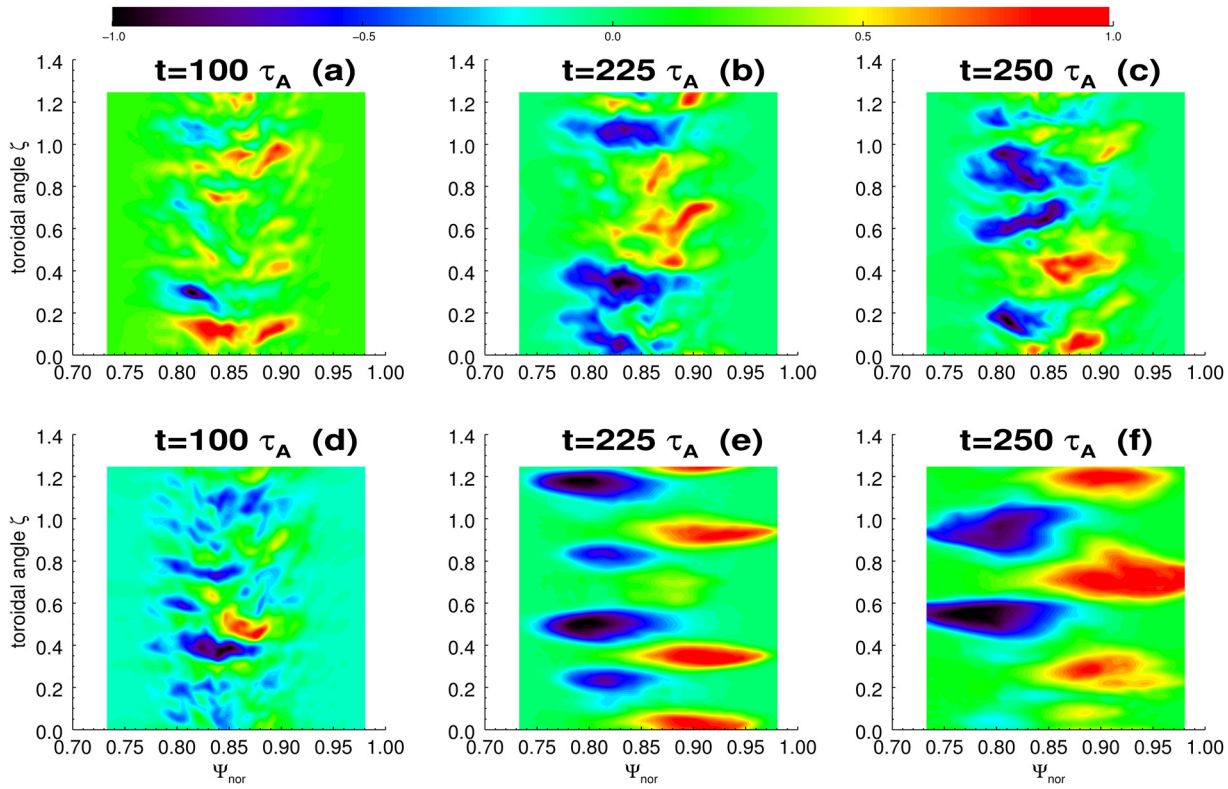

FIG. 9. Pressure perturbation pattern at the outer mid-plane for the case with $\alpha = 2.29$ (a)–(c) and the case with $\alpha = 2.44$ (d)–(f).

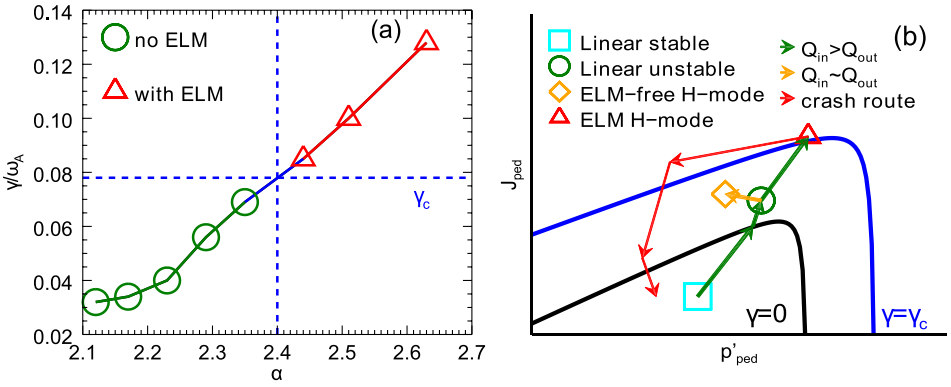

FIG. 10. (a) Maximum linear growth rate versus α; (b) schematic plot for ELM crash.

without ELMs. In this case, we get an ELM-free H-mode with a turbulent pedestal. So, the existence of ELM-free H-mode is a natural result of our nonlinear model. Moreover, the turbulent pedestal may generate different coherence patterns, which may explain the existence of coherent structure in ELM-free H-modes.

III. ELECTRON INERTIA AND HYPER-RESISTIVITY

During an ELM crash, fast reconnection occurs. Fast reconnection generates a narrow current layer (Fig. 11), which limits the utility of the simulation. Retaining the anomalous transport of current can resolve this problem. In a previous study, a constant hyper-resistivity was included in BOUT++ to model anomalous current transport.[7] The hyper-resistivity is not determined by the simulation itself and is based on theoretical estimates. A self-consistent simulation with self-generated hyper-resistivity is of great importance to the study of ELMs. Here, we report on our attempt to accomplish this by including electron inertia in P-B turbulence. Of course, other mechanisms may also be relevant in resolving the current layer, such as the parallel electron pressure in Ohm's law,[13,14] and we will study this issue by using our 6-field model.[15]

A. Linear impact of electron inertia

With the electron inertia, Ohm's law changes from that of Eq. (3) to

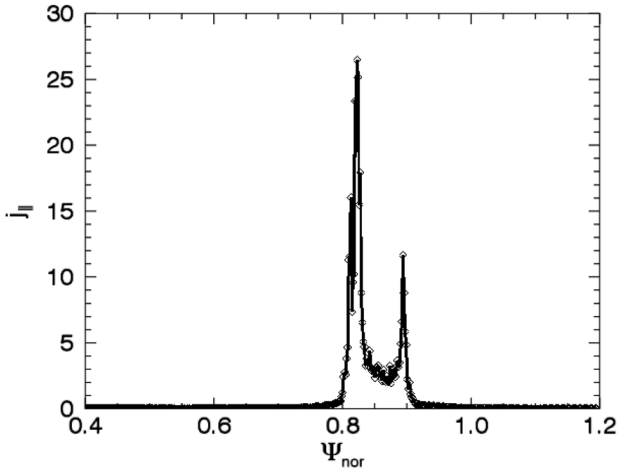

FIG. 11. The radial profile of current perturbation in nonlinear ELM simulations without hyper-resistivity.

$$-\frac{m_e}{e}\frac{\partial \tilde{u}_{\parallel e}}{\partial t}-\frac{m_e}{e}\mathbf{V}_{ET}\cdot\nabla\tilde{u}_{\parallel e}-\frac{m_e}{e}\mathbf{V}_E\cdot\nabla u_{\parallel e0}+\frac{\partial A_\parallel}{\partial t}$$
$$=-\partial_\parallel\phi_T+\frac{\eta}{\mu_0}\nabla_\perp^2 A_\parallel-\frac{\eta_H}{\mu_0}\nabla_\perp^4 A_\parallel. \quad (10)$$

It is widely known that electron inertia can weaken shear Alfvén stabilization and thus destabilize P-B modes.[16] This is easy to understand via a linear local analysis. Keep only the time derivative term with electron inertia and the linearized Eq. (12), we get

$$-\frac{m_e}{n_0\mu_0 e^2}\frac{\partial\nabla_\perp^2 A_\parallel}{\partial t}+\frac{\partial A_\parallel}{\partial t}=-\partial_\parallel\phi, \quad (11)$$

$$\hat{A}_\parallel=\frac{k_\parallel}{\omega(1+\delta_e^2k_\perp^2)}\hat{\phi}. \quad (12)$$

Here, $\delta_e=\sqrt{m_e/n_0\mu_0e^2}$ is the collision-less electron skin depth and $k_\perp^2=k_x^2+m^2/a^2$ is the perpendicular wave number. Substituting Eq. (12) into the linearized Eq. (1), we get

$$-i\omega\hat{\varpi}=\frac{1}{\mu_0}k_\parallel k_\perp^2\frac{k_\parallel}{\omega(1+\delta_e^2k_\perp^2)}\hat{\phi}+R.H.S.$$

Note that the first term on the RHS represents shear Alfvén stabilization from field line bending, which is reduced by a factor of $1/(1+\delta_e^2k_\perp^2)$ when electron inertia is included. The destabilizing effect of electron inertia decreases with increasing density. Our linear simulation results also verify this point. In Fig. 12, we can see when density is low, the destabilization effect is strong and when density is high, the destabilization is weak. For $n_0=10^{19}\,\mathrm{m}^{-3}$, $\delta_e=1.67\,\mathrm{mm}$. Note that the width of the resistive current sheet $\Delta_J\approx R\sqrt{\omega_A/(\gamma_{PB}S)}$ is about 10–100 microns and the width of hyper-resistive current sheet $\Delta_H\approx R(\omega_A/(\gamma_{PB}S_H))^{1/4}\sim 1.78\,\mathrm{mm}$ for $S_H=10^{12}$.[7] So the electron skin depth is comparable to the width of hyper-resistive current sheet. This is why the electron inertia may be able to generate enough current relaxation and replace the hyper-resistivity term in Ohm's law.

With electron inertia, the threshold is also reduced as shown in Fig. 13. For density as low as $n_0=10^{19}\mathrm{m}^{-3}$, the α value needed for an unstable mode is 10% smaller than the original case, while the shift is quite small for the high density case with $n_0=5\times10^{19}\mathrm{m}^{-3}$. Thus, even for the calculation of linear instability, electron inertia is important if the

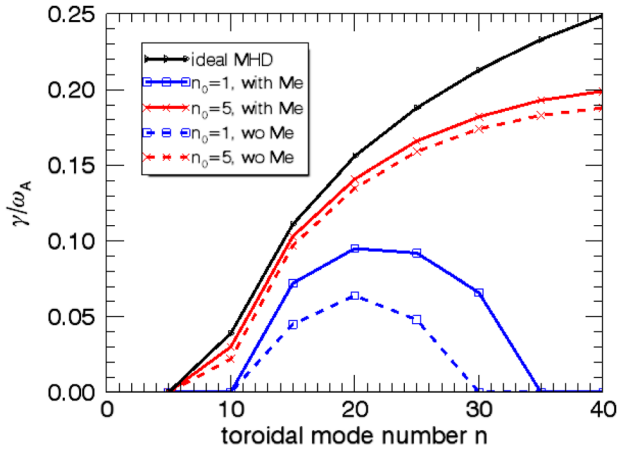

FIG. 12. Linear growth rates versus toroidal mode number for low density cases (blue) and high density cases (red). Solid curves are with electron inertia and dashed curves are without electron inertia. The solid black curve shows the ideal MHD calculation. The unit for the density is $10^{19}\mathrm{m}^{-3}$.

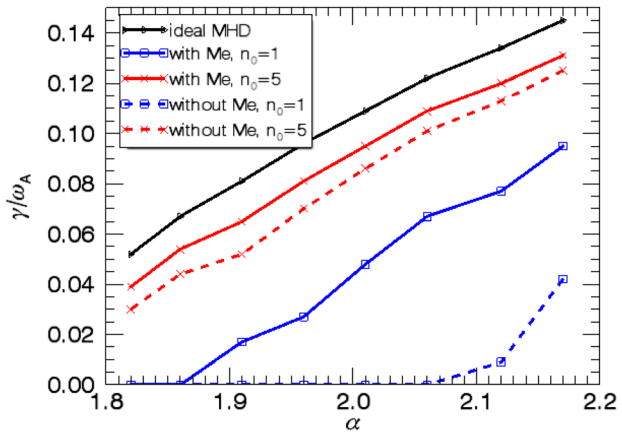

FIG. 13. Linear growth rate versus α for low density case with $n_0 = 10^{19}\mathrm{m}^{-3}$ (blue) and high density case with $n_0 = 5\times10^{19}\mathrm{m}^{-3}$ (red). Solid curves are without electron inertia and dashed curves are with electron inertia. The solid black curve shows the ideal MHD calculation. The unit for the density is $10^{19}\mathrm{m}^{-3}$.

density is low. This reminds us that in the analysis of the quiescent high (QH) confinement mode,[4] which is a low density regime, electron inertia should be retained.

Note that non-ideal effects, such as electron inertia and resistivity, can reduce the linear ideal MHD threshold, while the nonlinear effects increase the threshold. The ultimate result of non-ideal and nonlinear shifts on the threshold can be quite close to the ideal MHD boundary. Considering the experimental error bars, it is then not surprising that ideal MHD can fit the experimental results well. However, the underlying physics of the ideal MHD threshold and the nonlinear threshold is quite different.

B. Nonlinear simulation with electron inertia

The nonlinear electron current convection term is believed to be able to generate anomalous current transport if there is a certain level of background turbulence. According to our previous result, before the onset of ELMs, P-B turbulence is generated. Thus, it is interesting to see if the P-B turbulence can generate enough current transport for the pedestal to go through an ELM crash.

Here, we choose the case with $\alpha = 1.96$ with density $n_0 = 10^{19}\mathrm{m}^{-3}$. This case is stable to P-B modes, but unstable to electron inertial PB modes. From Fig. 14, we can see that the filament starts to appear and the perturbation extends radially. However, the simulation ultimately fails due to the formation of narrow current layers. In Fig. 15, the evolution of the radial spectrum of current is shown. At the last time step, we can see that strong high-kx components appear. This result shows that P-B turbulence alone is not sufficient to generate the necessary current transport. More quantitative measurement of the current transport during an ELM crash will be our next step. And it is also interesting to compare the current transport processes during an ELM crash with other physics process in plasmas, as described in Ref. 17.

Note that in the pedestal, there should be some ambient micro-turbulence,[18] like KBM turbulence or electron temperature gradient turbulence. Such micro-turbulence can also generate current relaxation. However, to self-consistently simulate such micro-turbulence in a MHD code is a great challenge. In particular, either a dynamic sub-grid scale model or a multiscale simulation is necessary.

IV. SUMMARY

In conclusion, we find that the triggering of an ELM crash is a nonlinear, random process, which depends on both linear growth rate $\gamma(n)$ and the statistical phase coherence time, $\tau_c(n)$. There is no purely deterministic criterion for the onset of ELMs available at this time. Over longer time scales, the onset of ELMs can be predicted by the probabilistic criterion $\gamma > \gamma_c \sim \ln 10/\bar{\tau}_c$. ELMs can be controlled by changing the growth rate spectrum or by shortening the PCT.

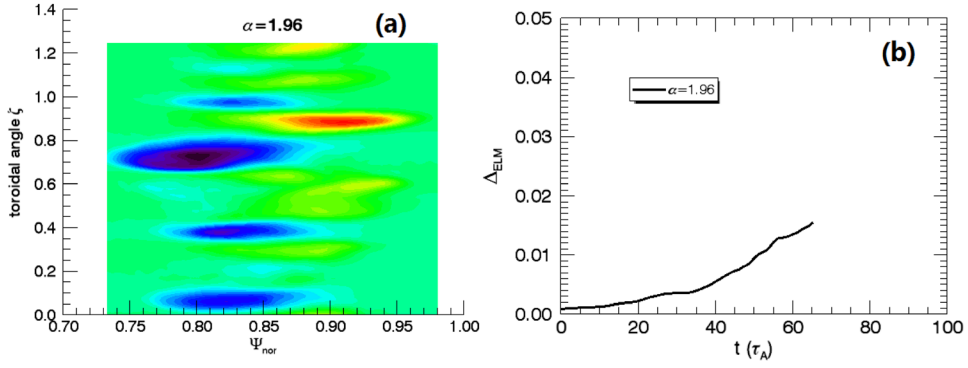

FIG. 14. (a) Pressure perturbation at the outer mid-plane; (b) time evolution of ELM size.

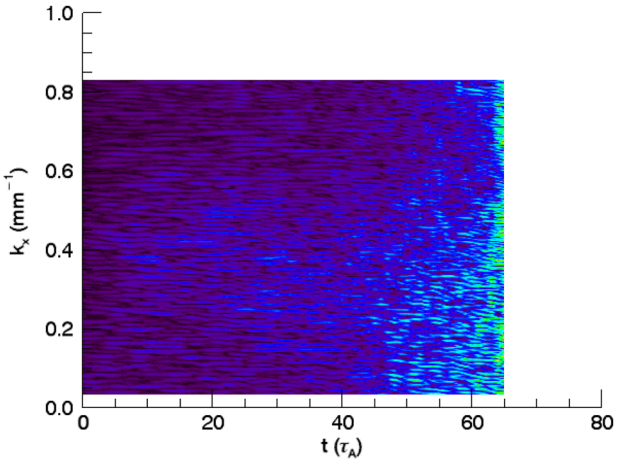

FIG. 15. Time evolution of radial spectrum of current perturbation.

The control of $\gamma(n)$ and $\tau_c(n)$ via flow shear, magnetic shear, or other equilibrium quantities, the spatial-temporal evolution of the relative phase and of $\tau_c(n)$, and also the effect of finite diffusion on phase evolution are all important issues to study in the future. More generally, this study points toward the key role of relative phase evolution in controlling bursty relaxation.

We also demonstrate that electron inertia must be retained in low density regimes like QH mode. However, a P-B turbulence alone with electron inertia cannot generate enough current transport. Thus, a nonlinear ELM simulation with self-consistent electron dissipation is intrinsically a multiscale problem.

ACKNOWLEDGMENTS

This work was performed under the auspices of the U.S. DoE by LLNL under Contract No. DE-AC52-7NA27344 and was supported by the NSFC under Grant Nos. 10935004 and 11261140326, the WCI program of Korea, and the CMTFO sponsored by the U.S. DoE. The authors wish to thank useful discussion with X. G. Wang, P. Snyder, F. L. Waelbroeck, H. Zohm, T. Y. Xia, and G. Dif-Pradalier.

[1]H. Zohm, Plasma Phys. Controlled Fusion **38**, 105 (1996).
[2]ITER Physics Expert Group, Nucl. Fusion **39**, 2391 (1999).
[3]P. B. Snyder, H. R. Wilson, J. R. Ferron, L. L. Lao, A. W. Leonard, T. H. Osborne, A. D. Turnbull, D. Mossessian, M. Murakami, and X. Q. Xu, Phys. Plasma **9**, 2037 (2002).
[4]P. B. Snyder, K. H. Burrell, H. R. Wilson, M. S. Chu, M. E. Fenstermacher, A. W. Leonard, R. A. Moyer, T. H. Osborne, M. Umansky, W. P. West, and X. Q. Xu, Nucl. Fusion **47**, 961 (2007).
[5]A. Burckhart, E. Wolfrum, R. Fischer, K. Lackner, H. Zohm, and ASDEX Upgrade Team, Plasma Phys. Controlled Fusion **52**, 105010 (2010).
[6]P. B. Snyder, R. J. Groebner, J. W. Hughes, T. H. Osborne, M. Beurskens, A. W. Leonard, H. R. Wilson, and X. Q. Xu, Nucl. Fusion **51**, 103016 (2011).
[7]X. Q. Xu, B. D. Dudson, P. B. Snyder, M. V. Umansky, and H. R. Wilson, Phys. Rev. Lett. **105**, 175005 (2010).
[8]X. Q. Xu, B. D. Dudson, P. B. Snyder, M. V. Umansky, H. R. Wilson, and T. Casper, Nucl. Fusion **51**, 103040 (2011).
[9]P. W. Xi, X. Q. Xu, and P. H. Diamond, Phys. Rev. Lett. **112**, 085001 (2014).
[10]P. W. Xi, X. Q. Xu, T. Y. Xia, W. M. Nevins, and S. S. Kim, Nucl. Fusion **53**, 113020 (2013).
[11]H. R. Wilson and S. C. Cowley, Phys. Rev. Lett. **92**, 175006 (2004).
[12]A. Kirk, B. Koch, R. Scannell, H. R. Wilson, G. Counsell, J. Dowling, A. Herrmann, R. Martin, M. Walsh, and MAST Team, Phys. Rev. Lett. **96**, 185001 (2006).
[13]A. Y. Aydemir, Phys. Fluids B **4**, 3469 (1992).
[14]R. G. Kleva, J. F. Drake, and F. L. Waelbroeck, Phys. Plasmas **2**, 23 (1995).
[15]T. Y. Xia, X. Q. Xu, and P. W. Xi, Nucl. Fusion **53**, 073009 (2013).
[16]T. Rafiq, G. Bateman, A. H. Kritz, and A. Y. Pankin, Phys. Plasmas **17**, 082511 (2010).
[17]A. Ishizawa and N. Nakajima, Phys. Plasmas **17**, 072308 (2010).
[18]E. Wang, X. Xu, J. Candy, R. J. Groebner, P. B. Snyder, Y. Chen, S. E. Parker, W. Wan, G. Lu, and J. Q. Dong, Nucl. Fusion **52**, 103015 (2012).